Stereo Photogrammetry Measurements of the Position and Attitude of a Nozzle-plume/Shock-wave Interaction Model in the NASA Ames 9- by 7- Ft Supersonic Wind Tunnel

Edward T. Schairer[1]
NASA Ames Research Center, Moffett Field, CA, 94035-1000

Laura K. Kushner[2] and Bethany A. Drain[3]
ACI/NASA Ames Research Center, Moffett Field, CA, 94035-1000

James T. Heineck[4], and Donald A. Durston[5]
NASA Ames Research Center, Moffett Field, CA, 94035-1000

Stereo photogrammetry was used to measure the position and attitude of a slender body of revolution during nozzle-plume/shock-wave interaction tests in the NASA Ames 9- by 7-Ft Supersonic Wind Tunnel. The model support system was designed to allow the model to be placed at many locations in the test section relative to a pressure rail on one sidewall. It included a streamwise traverse as well as a thin blade that offset the model axis from the sting axis. With these features the support system was more flexible than usual resulting in higher-than-usual uncertainty in the position and attitude of the model. Also contributing to this uncertainty were the absence of a balance, so corrections for sting deflections could not be applied, and the "wings-vertical" orientation of the model, which precluded using a gravity-based accelerometer to measure pitch angle. Therefore, stereo photogrammetry was chosen to provide independent measures of the model position and orientation. This paper describes the photogrammetry system and presents selected results from the test.

Nomenclature

c_x, c_y	=	image-plane scale factors in horizontal and vertical directions, pixels
H	=	height of model from pressure rail in model coordinates, in
K_1, K_2	=	first- and second-order symmetrical lens distortion correction factors
M	=	free-stream Mach number
m_{ij}	=	elements of 3-by-3 rotation matrix
NPR	=	nozzle pressure ratio
P_t	=	free-stream total pressure, psf
q	=	free-stream dynamic pressure, psf
X, Y	=	image-plane coordinates of target, corrected for lens distortion, pixels
X_d, Y_d	=	measured image-plane coordinates of target, pixels
X_p, Y_p	=	principal point, pixels
x, y, z	=	object-space coordinates in "wings vertical" tunnel axes, in origin at knuckle sleeve x positive downstream, y positive above centerline, z positive toward cameras
x_c, y_c, z_c	=	object-space coordinates of camera perspective center, in
α	=	angle of attack, °

[1] Aerospace Engineer, Experimental Aero-Physics Branch, MS 260-1, non-member.
[2] Research Engineer, ACI/Experimental Aero-Physics Branch, MS 260-1, non-member.
[3] Associate Engineer, ACI/Experimental Aero-Physics Branch, MS 260-1, non-member.
[4] Photographic Technologist, Experimental Aero-Physics Branch, MS 260-1, non-member.
[5] Aerospace Engineer, Experimental Aero-Physics Branch, MS 260-1, member.

subscripts

nom	=	nominal or “set” values of test parameters, often slightly different than true values
PG	=	measured by photogrammetry
SDS	=	measured by Standard Data System

I. Introduction

A slender body of revolution with a simulated jet engine and shock-wave generators at its aft end was tested in the 9- by 7-Ft Supersonic Wind Tunnel at NASA Ames Research Center.[1] The purpose of the test was to study interactions between shock waves from the shock generator and the exhaust plume from the simulated engine. These interactions are important because they are likely to occur on civil supersonic transports where they may have a large effect on the sonic boom. The principal measurement in the test was the near-field pressure signature from the model, which was measured by a pressure rail mounted to one sidewall of the test section. The model-support system allowed the model to be placed over a wide range of positions relative to the pressure rail. The model support, however, was less rigid than a conventional support system–it included a streamwise traverse mechanism and a thin, swept blade that offset the model axis from that of the sting–and it did not include a balance, so position and attitude data from the Standard Data System (SDS) could not be corrected for model loads. In addition, the model was tested with the pitch plane horizontal (the usual configuration in this wind tunnel), so a gravity-based accelerometer could not be used to measure angle of attack. For these reasons, an independent, supplementary method was needed to measure the model position and attitude, and stereo photogrammetry was selected for this purpose.

Stereo photogrammetry allows the positions of points in space to be determined from images of the points as seen by cameras from at least two directions. Each camera is calibrated to determine the transformation from 3-D object space to a 2-D image plane. The uncertainty of the measurement depends on the fidelity of these transformations; how accurately corresponding points can be located in the images; the number of views; and the angular separation between

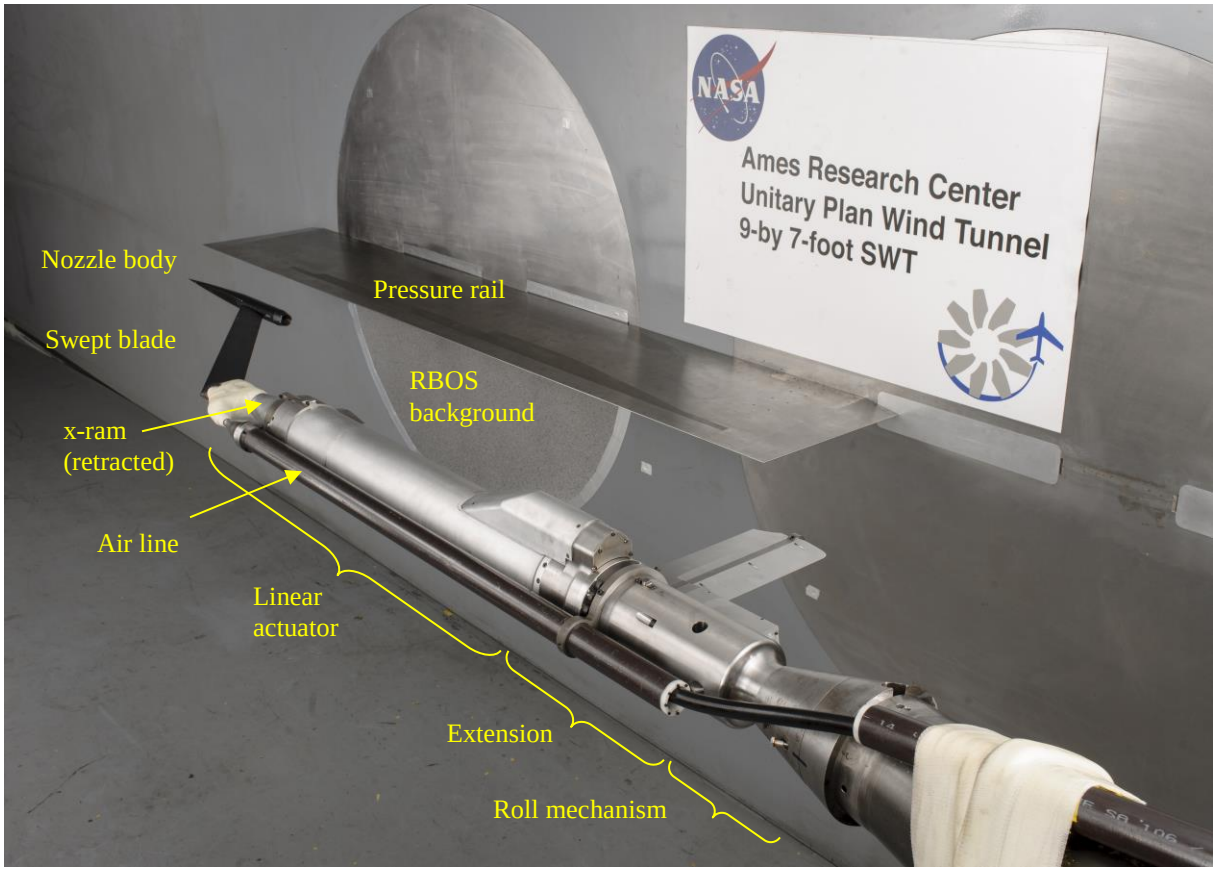

Figure 1. Nozzle-plume/shock-wave model installed in test section of 9- by 7-Ft Supersonic Wind Tunnel.

the views. Measurements of at least three rigidly connected, non-co-linear points are required to establish the position and orientation of an object in space.

The first documented use of stereo photogrammetry in a wind tunnel was in 1977 by Brooks and Beamish who used two film cameras to resolve aeroelastic deformations as small as 0.02 in of a swept-wing model in the 8-Ft Transonic Wind Tunnel at NASA Langley Research Center.[2] Today, with the availability of high-resolution digital cameras and ever more powerful computers, photogrammetry can yield accurate measurements in "real time." Practical constraints, however, can limit this potential. In particular, windows must be available in the test section that allow viewing the model from different directions with sufficient parallax. Markers or targets must be applied to the model that are durable, do not disturb the flow, and have high contrast with respect to the model surface so that their positions in the images can be determined automatically, without human intervention. The model must be lit so that the visibility of the targets is uniform and does not change as the model position and attitude changes. Glare from polished model surfaces can be particularly troublesome. Photogrammetry systems for measuring model position, attitude, and/or deformation have been deployed in wind tunnels around the world, including the National Transonic Facility (NTF) at NASA Langley Research Center[3] and the European Transonic Wind Tunnel (ETW).[4]

At Ames Research Center, interest in developing optical methods for measuring angle of attack and model deformation in the Unitary Plan Wind Tunnels (UPWT) dates back to the 1980's.[5-7] Recently this interest has been revived, and stereo photogrammetry has been used to measure model deformation in several tests in both the 11- by 11-Ft Transonic Wind Tunnel and the 9- by 7-Ft Supersonic Wind Tunnel.[8-9] These tests are relevant to the present test because model deformation measurements (MDM) also require measuring the position and attitude of the model to account for rigid-body movement.

This paper describes the photogrammetry system that was used to measure the model position and attitude in the present test and presents selected results.

II. Apparatus

A. Wind Tunnel and Test Section

The test was conducted in the 9- by 7-Ft Supersonic Wind Tunnel at NASA Ames Research Center. Mach numbers in the test section between 1.5 and 2.5 are set by sliding the lower half of a two-dimensional, asymmetric nozzle in the stream-wise direction, thereby altering the height of the sonic throat. The test section includes four large turntables, two in each sidewall, that can be fitted with 28.5-in dia eccentric windows for schlieren measurements. In addition, the turntables have cut-outs for smaller (6.25 in dia) windows where cameras and lamps can be placed. The sidewalls are flat and parallel whereas the top and bottom walls are contoured at their upstream ends to blend with the nozzle.

For the present test, a very narrow pressure rail was mounted along the centerline of one (north) sidewall (Fig. 1). The rail was 90 in long and extended 14 in outward from the wall. Four hundred and twenty static pressure taps were spaced at 0.157-in (4 mm) intervals along its outboard edge. To accommodate the pressure rail, it was necessary to fill the turntables in the north sidewall with solid blanks rather than windows, which precluded the use of conventional schlieren. Therefore, as an alternative, density gradients were visiualized by retro-reflective background-oriented schlieren (RBOS[10]) for selected cases. The lower half of the inside surface of one of these turntables was covered with a sheet of speckled retro-reflective material. This sheet appeared in the background of the model when illuminated and viewed through a window in the opposite sidewall.

B. Model

The model was of a slender body of revolution ("nozzle body") with a very sharp nose (Fig. 2). It was approximately 22 in long and its maximum cross-sectional diameter was 1.5 in. Interchangeable convergent-divergent nozzles (short, medium, and long) were attached to the downstream end of the nozzle body, and interchangeable shock-wave generators of various types ("bi-convex", "double wedge", "aft deck", "25-D tail") were attached to either the nozzle body or the blade that supported the model (Fig. 3).

The model was tested with the pitch plane horizontal, so the pressure rail on the north sidewall was immediately "below" the model in the model coordinate system. "Wings vertical" is the usual orientation for tests in this tunnel because it minimizes the effects of flow curvature on angle of attack. This curvature is mostly confined to vertical planes and is produced by the 2-D asymmetric nozzle upstream of the test section (Fig. 4).

Upstream of the sting, the model-support system (Fig. 1) included a roll mechanism, a sting extension, linear actuator and "x-ram" that allowed the model to be translated 24 in along its longitudinal axis (about one body length), and a forward-swept blade (sweep angle = 60°) that offset the model axis 12.5-in from the sting axis. High-pressure

air was fed to the model by a hose that was routed along the side of the sting and linear actuator and inside the blade. The blade was not particularly stiff in the lateral direction.

Figure 2. Nozzle body showing photogrammetry targets and pressure rail.

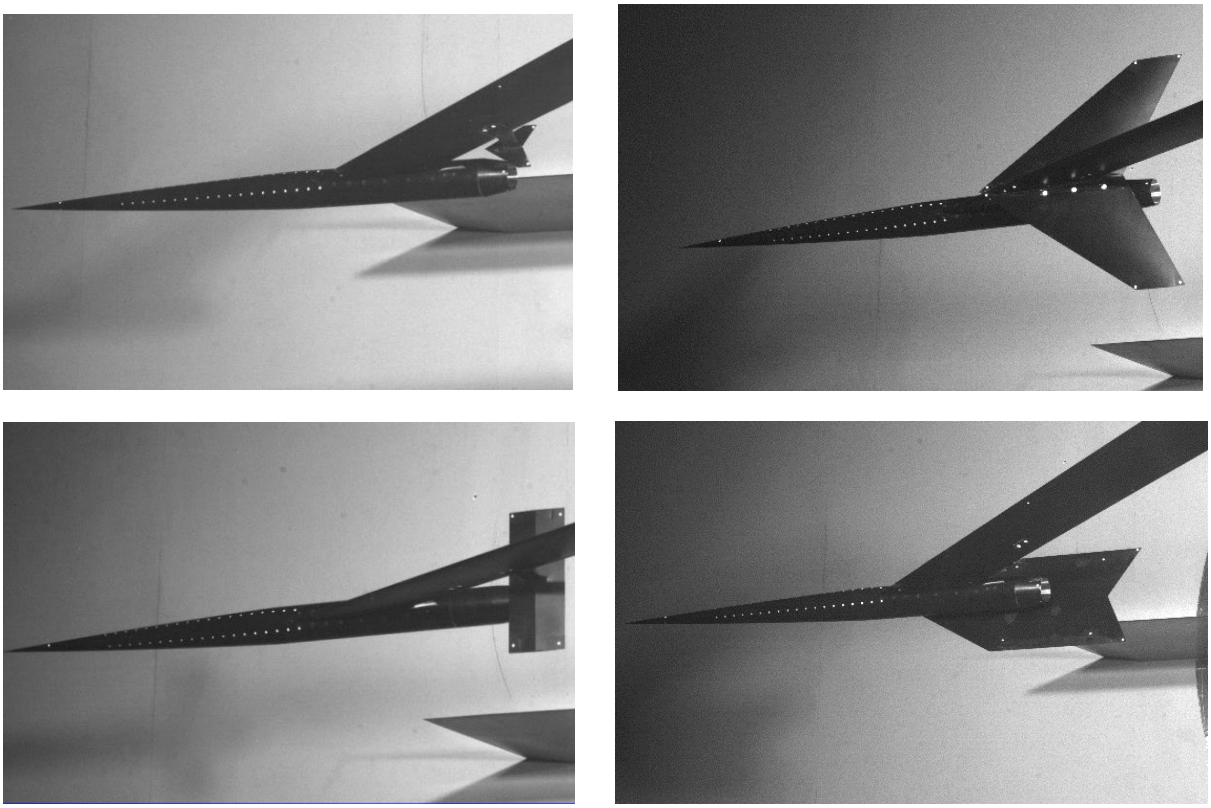

Figure 3. Nozzle body with shock-wave generators. *Biconvex tail (top-left); 25-D tail (top-right); double wedge (bottom-left); and aft deck (bottom-right).*

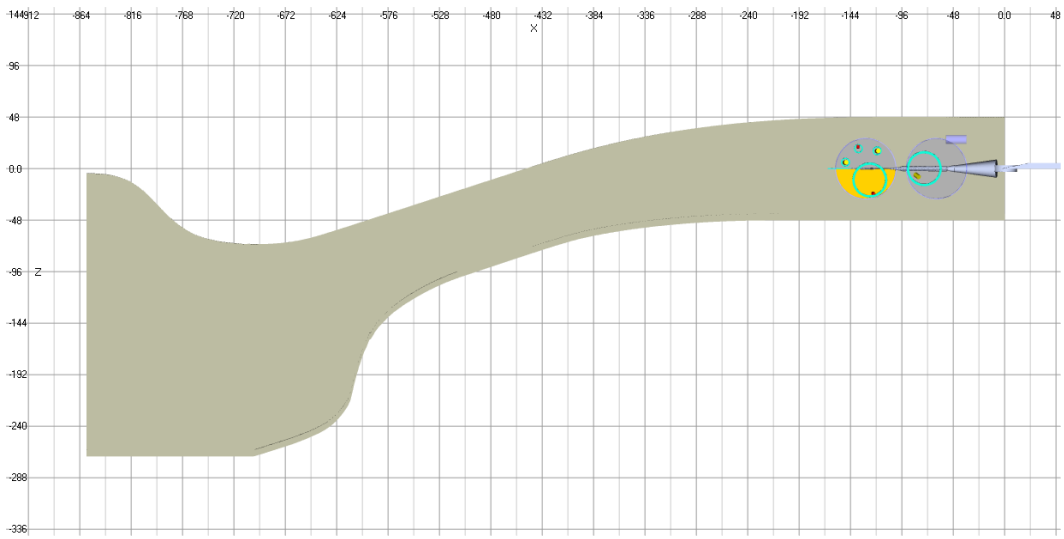

Figure 4. Asymmetric nozzle of 9- by 7-Ft Supersonic Wind Tunnel (*M* = 1.6). *Flow is left-to-right, test section is at upper right. Models are tested "wings vertical" to avoid effect of flow curvature on angle of attack.*

Models in the 9- by 7-Ft are supported by a horizontal strut that passes through both sidewalls of the diffuser. The strut can be driven laterally to move the model toward either sidewall, i.e., up or down in the model coordinate system. A "knuckle-sleeve" assembly is located at the leading edge of the strut and supports the sting. The knuckle-sleeve unit allows the sting to be oriented at any combination of pitch and yaw for which the resultant angle between the sting and the tunnel axis is less than or equal to 15°, i.e., within a cone with half-angle of 15°. Encoders and resolvers within the knuckle sleeve measure the angular positions of the knuckle and sleeve drive shafts from which angles of the sting in the vertical and horizontal planes are computed with uncertainties of about 0.05°.[11]

The model was coated with black inkjet ink that was applied with an artist airbrush. After the ink had dried the surface was buffed with 000 steel wool. A stencil was used to paint three longitudinal lines of white targets (dia = 0.1 in) at 0.5-in intervals along meridians separated by about 90° (Fig. 2).

C. Photogrammetry System

The photogrammetry system was designed using in-house virtual-imaging software.[12, 13] Figure 5 shows the range of model positions that had to be accommodated. Two high-resolution cameras (Imperx B6640; 6576 x 4384 pixels; pixel size = 5.5 μm) were mounted at windows in the sidewall opposite the pressure rail with the maximum vertical separation that the windows would allow (Fig. 6). The convergence angle between the cameras was about 38°. Wide-angle lenses (fl = 35 mm) were necessary to capture the model over its full range of positions and attitudes. The cameras were connected by fiber optic cables to a National Instruments PXI chassis. Data were acquired automatically using a LabVIEW program written in-house that was automatically triggered by the wind tunnel Standard Data System (SDS). The model was illuminated by three Dyna-Lite flash lamps (Model 2040) that were mounted at windows in the turntable and triggered by the camera strobe output (Fig. 6).

The cameras were calibrated after they were positioned, pointed, and focused. The calibrations were based on the collinearity equations of photogrammetry, which map each point in 3-D object space *(x, y, z)* to a point in the 2-D image plane (*X, Y*) using a simple pinhole representation of the camera:[14]

$$X = X_p - c_x \left[\frac{m_{11}(x - x_c) + m_{12}(y - y_c) + m_{13}(z - z_c)}{m_{31}(x - x_c) + m_{32}(y - y_c) + m_{33}(z - z_c)} \right]$$
$$Y = Y_p - c_y \left[\frac{m_{21}(x - x_c) + m_{22}(y - y_c) + m_{23}(z - z_c)}{m_{31}(x - x_c) + m_{32}(y - y_c) + m_{33}(z - z_c)} \right] \quad (1)$$

The principal point (X_p, Y_p) is where the optical axis passes through the image plane; c_x and c_y are scale factors in the horizontal and vertical directions of the image, respectively (approximately equal to the lens focal length in pixels);

(x_c, y_c, z_c) is the position of the camera "perspective center" in 3-D object space; and m_{ij} are elements of the 3- by-3 rotation matrix that is defined by the camera pointing angles.

Equation (1) assumes that image coordinates (X, Y) are free of lens distortion. Measured image coordinates (X_d, Y_d) were corrected for symmetrical lens distortion by:

$$X = X_d - K_1(X - X_p)r^2 - K_2(X - X_p)r^4$$
$$Y = Y_d - K_1(Y - Y_p)r^2 - K_2(Y - Y_p)r^4 \quad (2)$$

where $r^2 = (X - X_p)^2 + (Y - Y_p)^2$, and K_1 and K_2 are calibration constants

Taken together, the principal point (X_p, Y_p), scale factors (c_x, c_y,) and lens distortion constants (K_1, K_2) are the "internal orientation" of the camera. Their values were determined from images acquired while hand-holding a planar calibration plate with a rectangular array of targets (Fig. 7) at various angles relative to the cameras.[15] Because the cameras viewed the calibration plate through the test section windows, distortions due to the windows were accounted for in the calibration.

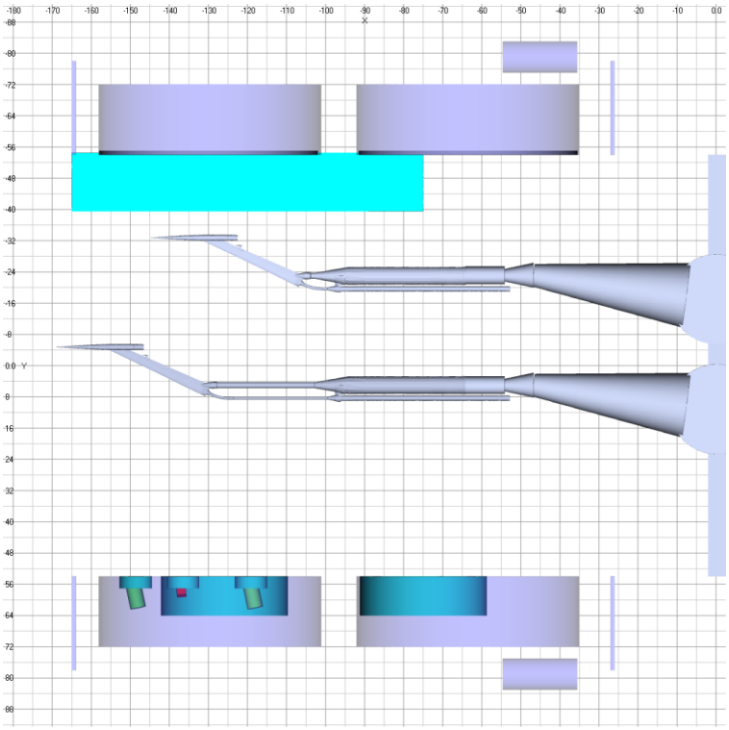

Figure 5. Top view of test section showing range of model positions. *Flow is left-to-right.Cameras and lamps are at bottom-left.*

The coordinates of the perspective center (x_c, y_c, z_c) and the rotation matrix (m_{ij}) define the "external orientation" or "pose" of each camera. They were determined by acquiring images of magnetic retro-reflective targets that were placed on the test section walls (floor, ceiling, and sidewall opposite the cameras, Fig. 8). The spatial positions of these targets were measured using a commercial photogrammetry system (V-STARS[16]). Beginning with an initial guess of the six pose parameters, the image-plane coordinates of the wall targets were computed by Eq. 1 using the known internal orientation of each camera. These coordinates were compared to the coordinates observed in the images, and the pose of each camera was iteratively adjusted until differences between the observed and computed coordinates were minimized. This is a nonlinear least-squares optimization problem that was solved using the Levenberg-Marquardt algorithm.[17] The algorithm does not converge if the initial guess is poor. A good guess was obtained by first computing the Direct Linear Transformation[18] (DLT, an approximate formulation of the collinearity equations) from the image- and object-space coordinates of the wall targets. Then, starting values for the six pose parameters were computed from the coefficients of the DLT.[14] This approach required at least six wall targets that were not all on the same wall.

III. Data Acquisition

Data acquisition typically involved placing the model at the desired attitude and distance from the pressure rail and then extending the x-ram longitudinally in 25 equal steps (making up one *x*-sweep or "SigSet"). Step sizes were even multiples of the spacing between orifices on the pressure rail (4 mm); the largest steps were six intervals (24 mm) and the smallest steps were one (4 mm). At the end of each step a trigger signal was sent by the Standard Data System (SDS) to the camera/lamp controller which then automatically triggered the cameras and lamps. Ten images were acquired from each camera at each test point at a frequency of 3.2 Hz (limited by the flash re-charge time).

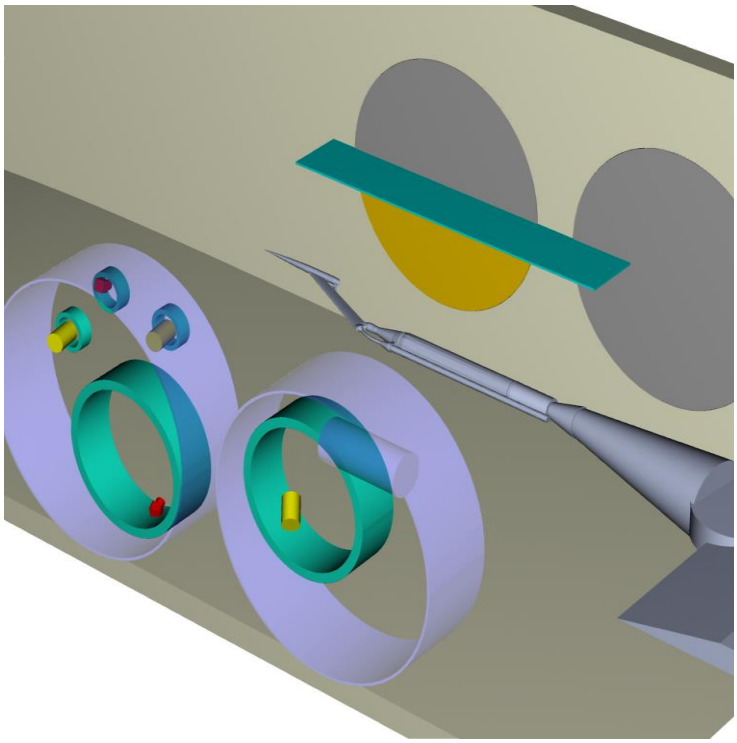

Figure 6. Layout of photogrammetry system. *Cameras are red, lamps are yellow.*

Reference images of the model were acquired at wind-off conditions with the model at zero pitch, yaw, and roll angles as measured by the SDS. The model was at its most downstream position (x-ram fully retracted, x = -149 in) and at H_{nom} = 8 in and y_{nom} = 0. The model configuration was the nozzle body only. This single wind-off condition was used as the reference for all wind-on conditions.

IV. Data Reduction

The image data were processed using photogrammetry software developed in-house. The approach was to compute the object-space coordinates of targets on the model from each pair of wind-on images and to compare these coordinates to the coordinates of the targets computed at the reference-zero wind-off condition. Then, the wind-on coordinates were translated and rotated as a rigid body to give the best fit to the wind-off coordinates. This is a nonlinear, least-squares problem that was solved by the Levenberg-Marquardt algorithm. The rotations that gave the best fit were assumed to be the instantaneous wind-on angles of the model. This calculation was repeated for each of the ten pairs of images at each test condition from which average and standard deviations of the model attitude and position were computed.

The photogrammetry measurements were not entirely independent of the SDS because the reference-zero condition was defined by SDS. The photogrammetry measurements would have been completely independent of SDS if theoretical (or, better yet, "as-built") body-axis coordinates of the targets had been used as the zero reference instead of coordinates measured at the SDS-defined zero condition. This approach was not used because neither theoretical nor as-built coordinates of the targets was available at the time of the test.

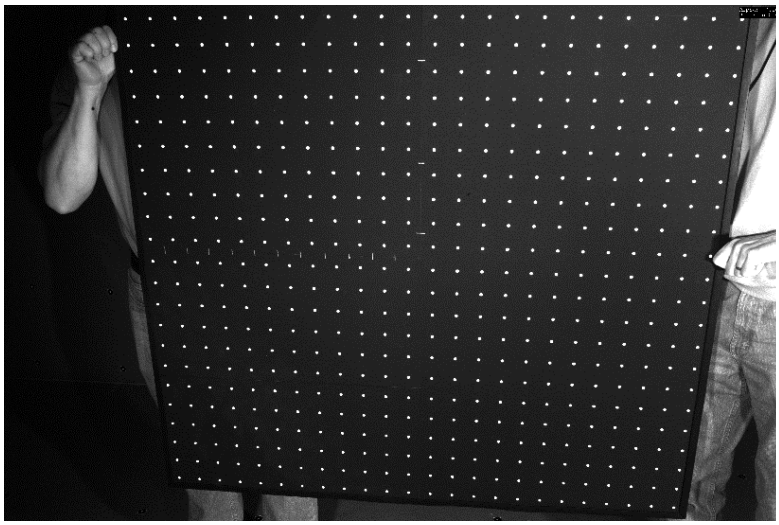

Figure 7. Image of hand-held calibration plate used for internal orientation.

Targets in the images were located by a semi-automatic procedure. The approximate locations of targets in the reference wind-off images were determined manually by point-and-click with the computer mouse. These approximate coordinates were then automatically refined using a centroid-finding algorithm. Since a single pair of wind-off images was used as a reference for all wind-on images, this manual procedure needed only to be done once. Point-and-click was also used to assist finding targets in the first-of-ten wind-on images from each camera; however, only two targets needed to be located in this way, one far forward and the other far aft on the model. Differences between the

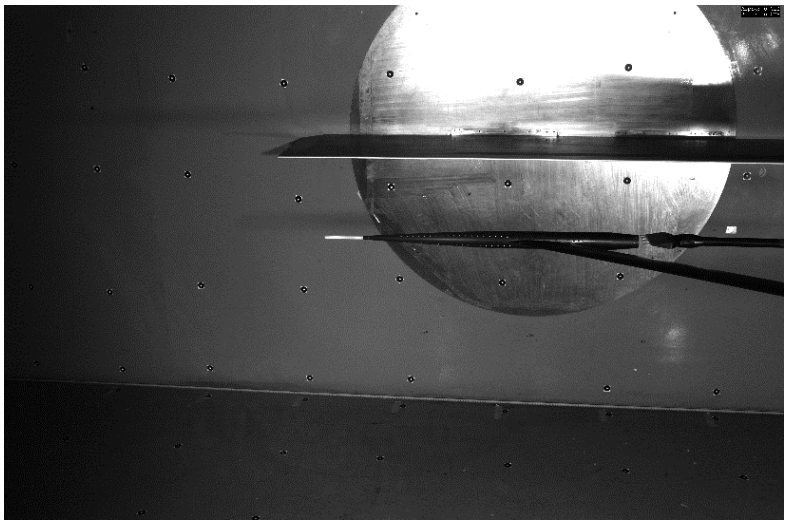

Figure 8. Image with retro-reflective wall targets used for external orientation.

wind-off and wind-on image-plane coordinates at these two targets were used to estimate the positions of all other targets in the wind-on image. The automatic centroid-finder then searched for each target in a small window centered on each estimated location, and refined target coordinates were written to a data file. The refined target coordinates in the first image from each camera were used as the starting point for locating all targets in images two through ten.

Including manual steps in the target-finding procedure meant that the angle and position measurements could not be made in real time or even near-real time. The data-reduction software includes a fully automatic algorithm for reading images and locating targets. For this algorithm to work reliably, however, the targets must be very distinct, the background must be very uniform, and the contrast between the targets and the background should be high. In the present test, the RBOS background appeared directly behind the model in many images, and the requirements of this background for RBOS—high-contrast, random speckles—was completely opposite to what was needed for reliable target finding. Therefore, when the search window included the RBOS background, the target-finding algorithm was very likely to fail. In addition, because of the wide range of model positions, the targets were often viewed very obliquely by one of the cameras, and at extreme positions contrast was low because lighting was not optimal. Bright highlights on the nozzle body also caused frequent errors in finding the targets. In cases where the target-finder failed, the target coordinates were manually edited.

After the image-plane coordinates of all targets were measured in images from both cameras and corrected for lens distortion, the space coordinates of each target were computed by combining the collinearity equations for both cameras and rearranging terms to form a set of four linear equations and three unknowns (x, y, z):

$$\begin{bmatrix} a_1^A & a_2^A & a_3^A \\ a_4^A & a_5^A & a_6^A \\ a_1^B & a_2^B & a_3^B \\ a_4^B & a_5^B & a_6^B \end{bmatrix} \begin{bmatrix} x \\ y \\ z \end{bmatrix} = \begin{bmatrix} a_1^A x_c^A + a_2^A y_c^A + a_3^A z_c^A \\ a_4^A x_c^A + a_5^A y_c^A + a_6^A z_c^A \\ a_1^B x_c^B + a_2^B y_c^B + a_3^B z_c^B \\ a_4^B x_c^B + a_5^B y_c^B + a_6^B z_c^B \end{bmatrix} \tag{3}$$

where

$$\begin{aligned} a_1 &= (X - X_p)m_{31} + c_x m_{11} \\ a_2 &= (X - X_p)m_{32} + c_x m_{12} \\ a_3 &= (X - X_p)m_{33} + c_x m_{13} \\ a_4 &= (Y - Y_p)m_{31} + c_y m_{21} \\ a_5 &= (Y - Y_p)m_{32} + c_y m_{22} \\ a_6 &= (Y - Y_p)m_{33} + c_y m_{23} \end{aligned}$$

Superscripts A and B indicate top and bottom cameras, respectively. Equation 3 is an over-determined set of linear equations that was solved in a least-squares sense for (x, y, z).

After the spatial coordinates (x, y, z) of the targets were computed from Eq. (3), the "re-projection error" for each target in each image was computed by substituting these coordinates into Eq. (1) and comparing the computed image-plane coordinates (X, Y) to the measured coordinates (after correcting for lens distortion). Typically this error was about one pixel or less; errors much larger than this usually indicated that the corresponding target had not been correctly located in one of the images.

The SDS measurements were based on encoder and resolver read-outs from the knuckle sleeve and linear actuator.[11] The data were not corrected for deformation of the support system because, without a balance, loads on the model were unknown.

V. Results

The test include 163 x-sweeps or "SigSets." Each sweep was characterized by the following parameters: model configuration (nozzle body alone or nozzle body with each of four shock-wave generators; free-stream flow condition (M = 1.6, P_t = 1800 psf, q = 759 psf or M = 2.0, P_t = 2100 psf, q = 751 psf); model attitude (α_{nom} = 0°, 1°, or 3°, yaw, roll); nozzle pressure ratio (NPR = 1 to 14 where NPR = 1 was no flow); longitudinal step size (4 to 24 mm) and number of steps (usually 25); and the horizontal distance of the model from the pressure rail (H_{nom} = 8 to 35 in), where, in the wings-vertical model coordinates, H was the distance of the model "above" the pressure rail. For most x-sweeps, yaw, roll, and the lateral position of the model (y) were all zero.

Photogrammetry images from 104 of the 163 x-sweeps were analyzed. For most of these sweeps, model position and attitude were not computed at all 26 longitudinal positions but only at the most upstream, and downstream positions and at a set (usually five or seven) of equally spaced positions in between. However, for a dozen sweeps the images were analyzed at all 26 positions. It was not practical to analyze all images from all sweeps because the automatic target-finding algorithm often failed and errors had to be corrected manually–a painfully slow process.

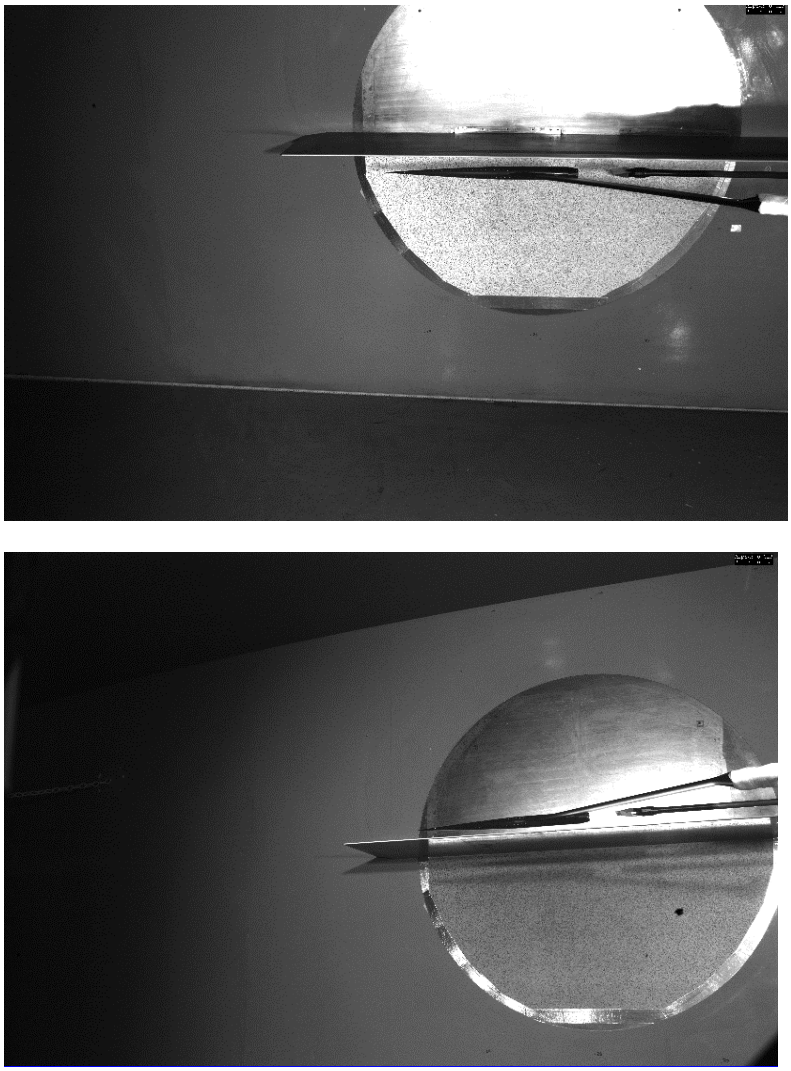

Figure 9. Typical images from upper (top) and lower (bottom) cameras. *Flow is left-to-right. The model is at the full downstream position.*

Figure 9 shows typical images from the two cameras. The model does not nearly fill the field of view—a necessary consequence of having fields of view large enough to capture the model over its full range of positions. Resolution of the model was 50–70 pixels/in, depending on the model position. Note that in the image from the top camera the model was directly in-front of the speckled RBOS background resulting in frequent target-finding errors. The RBOS background never appeared behind the model in images from the lower camera, so automatic target-finding in these images was much more successful.

Streamwise position (x), angle of attack (α), and distance from the rail (H) were the parameters measured by photogrammetry that had the largest effect on the pressure signature at the pressure rail. Angle of attack, H, and y were the parameters most likely to be affected by deflections of the model-support system. We begin by presenting photogrammetry and SDS measurements of angle of attack (α), distance from the rail (H), and lateral position (y) versus streamwise position (x) for x sweeps for the simplest, most symmetric, baseline model configuration—the nozzle body alone at α_{nom} = 0° and NPR = 1 (no blowing).

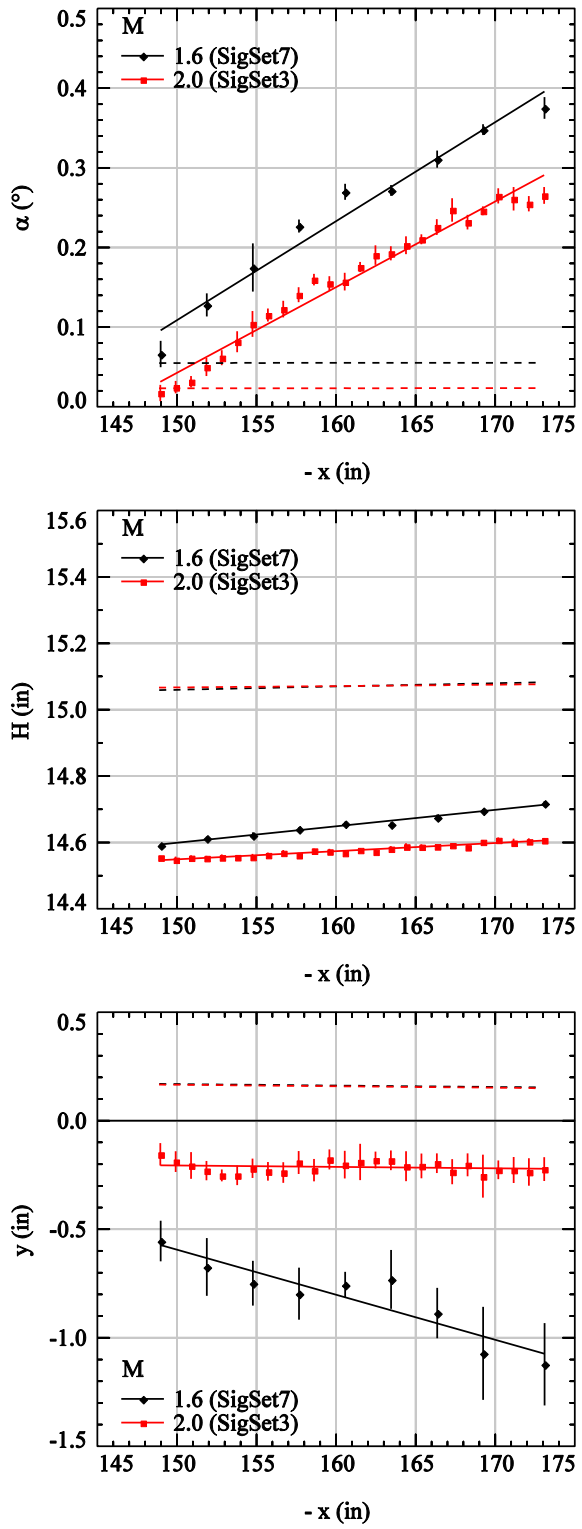

Figure 10. Measured α (top), *H* (center), and y (bottom) versus *x* at *M* = 1.6 and 2.0. *Nozzle body only, α_{nom} = 0°, H_{nom} = 15 in, NPR = 1.Dashed lines are SDS data.*

We then show the effects of blowing (NPR > 1), angle of attack (α_{nom}), the addition of shock generators, and distance of the model from the pressure rail (H_{nom}). Wherever possible, we compare cases where only one of the test parameters is different. The test matrix, however, was not designed with this in mind, so such simple comparisons were not always possible."Nominal" values of α, *H*, and *y* were based on SDS readouts.

Figure 10 shows α, *H*, and *y* versus streamwise position (*x*) for the baseline configuration (nozzle body alone, α_{nom} = 0°, NPR = 1, H_{nom} = 15 in) at *M* = 1.6 and 2.0. The symbols and error bars show the average and two standard deviations, respectively, of the ten instantaneous photogrammetry measurements at each position. Color-coordinated dashed lines show the corresponding SDS measurements. Small differences in actual settings between SigSets at the same nominal condition are reflected in the SDS data. Upstream is to the right, downstream to the left. The photogrammetry measurements at both Mach numbers indicate that α_{PG} increased linearly by about 0.3° between the most downstream and upstream positions whereas the SDS measurements indicated constant α (Fig. 10, top). The distance of the model from the rail (H_{PG}) also increased linearly as the x-ram was extended while H_{SDS} increased very slightly (Fig. 10, middle). There is also an offset of nearly 0.5 in between the photogrammetry and SDS measurements of *H*. Photogrammetry indicates that the model was offset slightly below the tunnel centerline ($y_{PG} < 0$) at both *M* = 1.6 and 2.0 (Fig. 10, bottom). At *M* = 1.6, however, this offset increased as the model moved upstream, whereas at *M* = 2.0 the offset remained nearly constant. The SDS data indicate that the model remained at a small offset above the tunnel centerline ($y_{SDS} > 0$). The standard deviations of the photogrammetry measurements (error bars in Fig. 10) were about ten times larger for *y* than for *H*. This reflects the much greater flexibility of the model support in the lateral direction (the out-of-plane direction of the thin swept blade), which resulted in large lateral oscillations of the model. The trends illustrated in Fig. 10 (bottom) were typical of all x sweeps.

The effects of blowing through the nozzle on α and *H* are shown at both *M* = 1.6 and 2.0 for the nozzle body alone at α_{nom} = 0° and H_{nom} = 15 in Fig. 11. Blowing created an offset in α_{PG} compared to the no-blowing case (NPR = 1) at both Mach numbers but did not change the slope $\Delta\alpha_{PG} / \Delta x$. The distance of the model from the rail (H_{PG}) also increased as the model moved upstream, and there was a slight increase in slope $\Delta H_{PG} / \Delta x$ with blowing, especially at *M* = 2.0, where NPR was highest. At *M* = 1.6 and NPR = 14 (Fig. 11 bottom-left), both photogrammetry and SDS show values for *H* that deviated from the otherwise linear trends at the three most downstream positions. Blowing had very little effect on *y* (not shown).

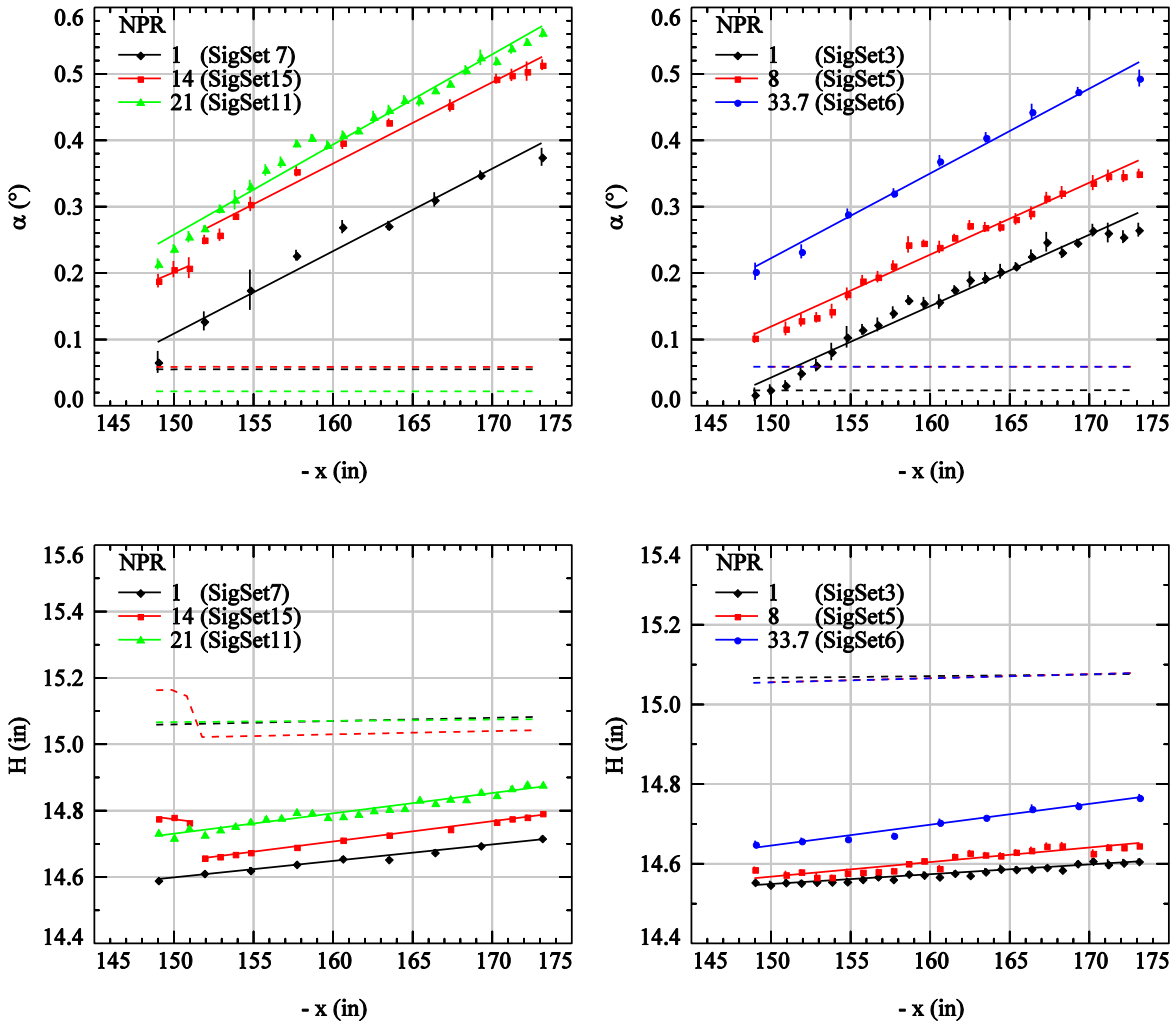

Figure 11. Effect of NPR on α (top) and *H* (bottom). *Nozzle body only; M = 1.6 (left) and M = 2.0 (right); α_{nom} = 0°; H_{nom} = 15.Dashed lines are SDS measurements.*

Figures 12 shows measurements of α and *H* for the nozzle body alone at two angles of attack (α_{nom} = 0° and 3°) where all other conditions are the same (*M* = 1.6, H_{nom} = 15 in, NPR = 21). At both angles α increased at approximately the same rates as the model moved upstream. The difference between the photogrammetry angle measurements at the two angles is very close to the SDS value of 3°. At α_{nom} = 3°, the model distance from the pressure rail (*H*) increased significantly as the model moved upstream. This is expected because the x-ram was also inclined at 3° relative to the rail. The magnitude of the displacement (ΔH_{PG} = 1.465 in), however, was about 0.2 in greater than what can be accounted for by the 3° angle of the x-ram. This additional displacement was also larger than the displacement (ΔH_{PG} = 0.14 in) between the most upstream and downstream positions at α = 0°, indicating a larger load in the pitch plane.

The repeatability of the photogrammetry measurements is indicated in Fig. 13, where α and *H* are shown for the nozzle body only at *M* = 2.0, α_{nom} = 0°, H_{nom} = 15 in, and NPR = 8. Two of the data sets are from the beginning of the test program one day apart; the third set is from the end of the test, twelve days later. Measurements of H_{PG} between the three sets are within 0.1 in of each other, and measurements of α_{PG} are within about 0.04°.

The effects of the distance of the model from the pressure rail (H_{nom}) on the measured angle of attack (α) are shown in Fig. 14 for the nozzle body alone at *M* = 2.0, α_{nom} = 0°, NPR = 8. For all three values of H_{nom}, α_{PG} increased as the model moved upstream, and the rate of increase was approximately the same. The same behavior was also observed at *M* = 1.6 (not shown).

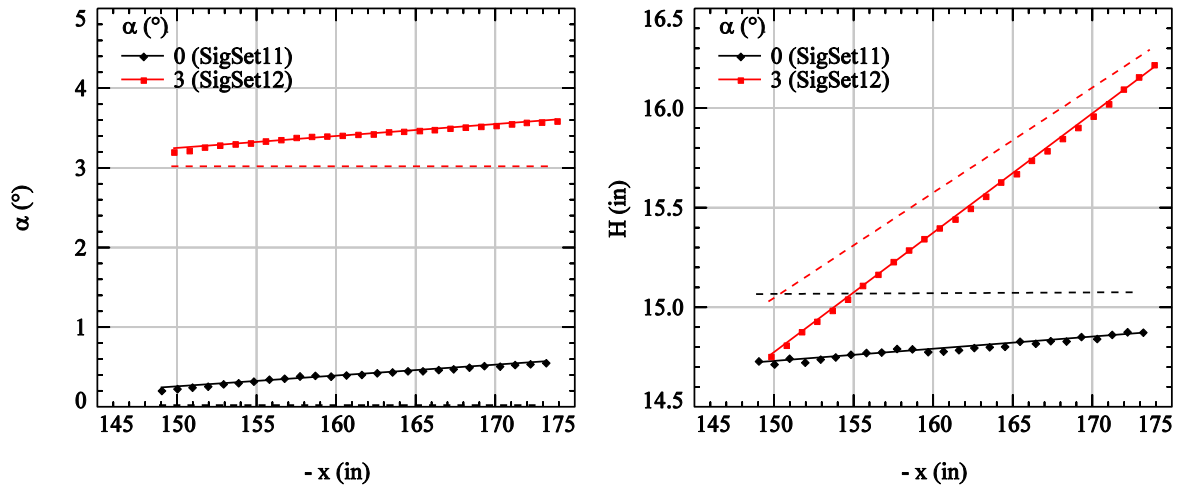

Figure 12. Measured α and *H* at α_{nom} = 0° and 3°. *Nozzle body alone, M = 1.6, H_{nom} = 15 in; NPR = 21.*

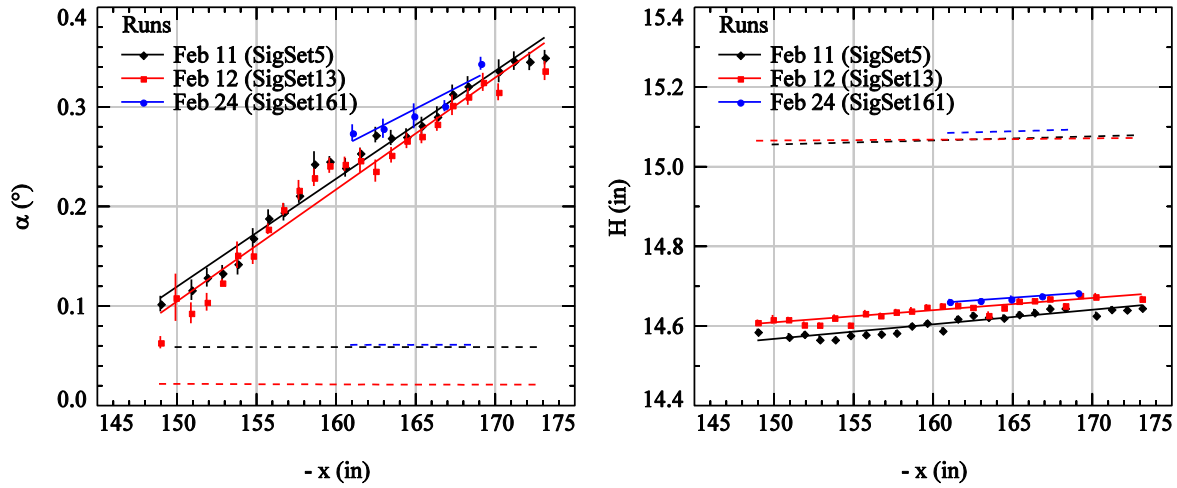

Figure 13. Repeatability of data. *Nozzle body alone; M = 2.0; α_{nom} = 0°; H_{nom} = 15 in; NPR = 8.*

Adding the very small biconvex tail had little or no effect on α, as shown in Fig. 15 (left) for M = 1.6, α_{nom} = 0°, H_{nom} = 15 in, and NPR = 1 (no blowing). In contrast, the much larger aft deck (Fig. 15, right) increased α_{PG} compared to the nozzle body alone, other things being equal (M = 2.0, α_{nom} = 0°, H_{nom} = 15 in, and NPR = 1); however, the slope $\Delta\alpha_{PG}$ / Δx did not change. Figure 16 compares α versus x for three of the four shock-wave generators (biconvex tail, 25-D tail, and aft deck) and the nozzle body alone, all at the same condition (M = 1.6, α_{nom} = 0°, H_{nom} = 15 in, NPR = 8). The measured α_{PG} versus x for the biconvex tail and 25-D tail configurations were nearly the same as for the nozzle body alone. For the aft deck configuration the measured α_{PG} was greater than for the nozzle body alone.

Finally, α versus x measurements of the double-wedge configuration are shown in Fig. 17 at three values of H_{nom} with all other parameters the same (M = 2.0, α_{nom} = 0°, NPR = 10). α_{PG} increased with distance upstream at all three heights, but the rate of increase was lower at the upstream positions.

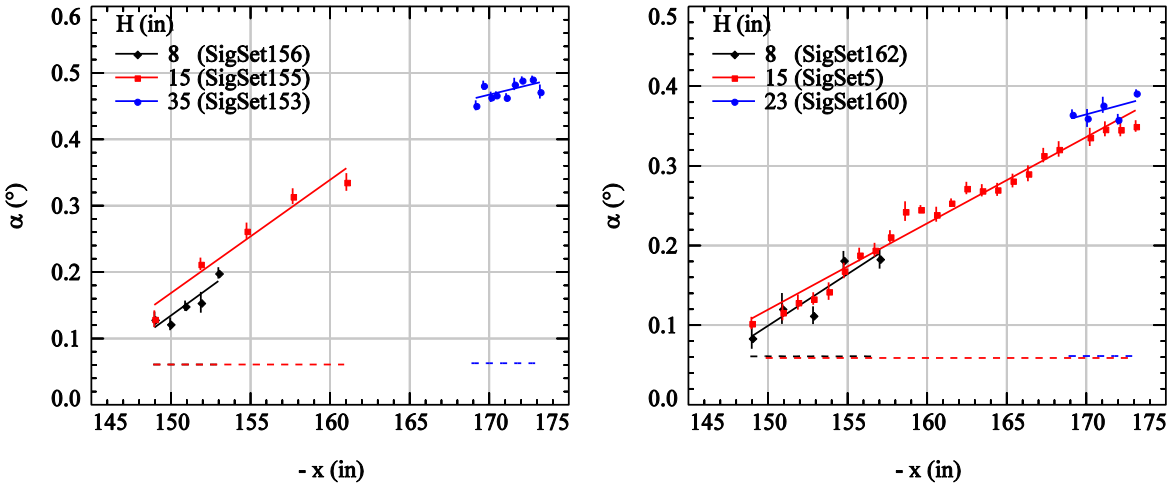

Figure 14. Effect of H_{nom} on α. *Nozzle body alone; M = 1.6 (left) and 2.0 (right); α_{nom} = 0°; NPR = 8.*

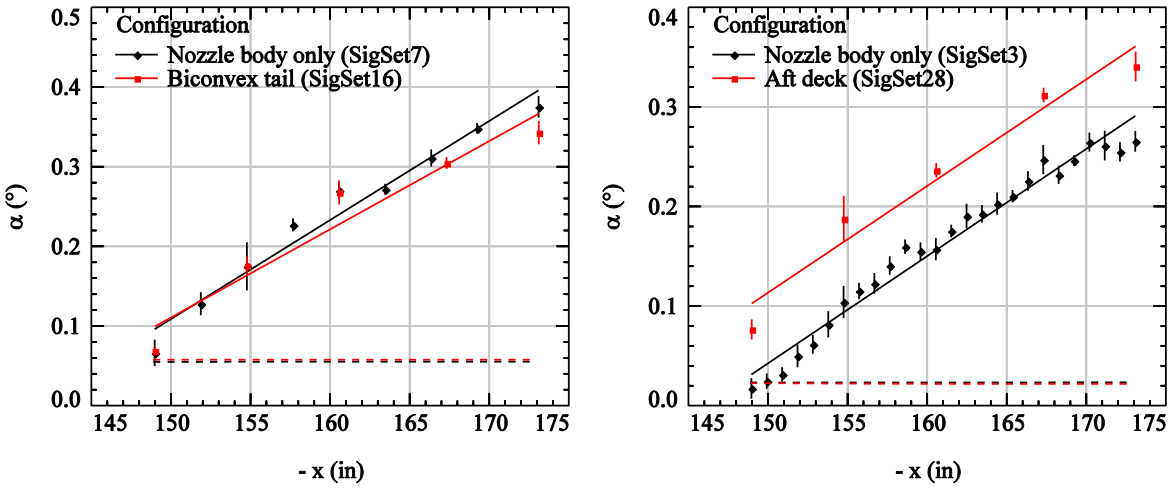

Figure 15. Effect of shock-wave generators on α (α_{nom} = 0°; H_{nom} = 15 in; NPR = 1). *Left: Biconvex tail, M = 1.6: Riaht: Aft deck. M = 2.0.*

VI. Discussion

There are clear trends in the photogrammetry and SDS measurements. For each x-sweep, both α_{PG} and H_{PG} increased in a nearly linear manner as the model moved upstream. This occurred even for the most symmetric configuration—the nozzle body alone at α_{nom} = 0° and no blowing (Fig. 10). For α_{nom} = 3°, ΔH_{PG} was slightly larger than the displacement due to the angle of the x-ram. In contrast, there was little or no change in α_{SDS}, H_{SDS}, or y_{SDS} during all sweeps at α_{nom} = 0°, a result expected for constant settings of the knuckle-sleeve and in the absence of corrections for sting deflections. For α_{nom} = 3°, H_{SDS} increased by nearly exactly the amount expected due to the angle of the model and x-ram (Fig. 12).

There was a consistent offset between H_{PG} and H_{SDS}: photogrammetry placed the model as much as 0.5 in closer to the pressure rail than SDS at all streamwise positions. Photogrammetry also consistently placed the model slightly below the tunnel centerline (y_{PG} < 0, the direction of gravity) whereas y_{SDS} was always very close to zero (for y_{nom} = 0). Also notable was a consistent difference in y_{PG} vs x at M = 1.6 and 2.0: at M = 1.6 y_{PG} became increasingly negative as the model moved upstream; at M = 2.0 y_{PG} was more nearly constant (e.g., Fig. 10, bottom). Blowing (NPR > 1)

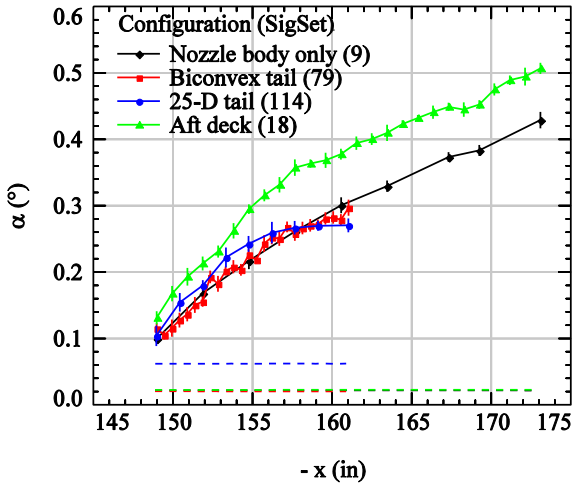

Figure 16. Effect of shock-wave generators on α.
M = 1.6; α_{nom} = 0°; H_{nom} = 15 in; NPR = 8.

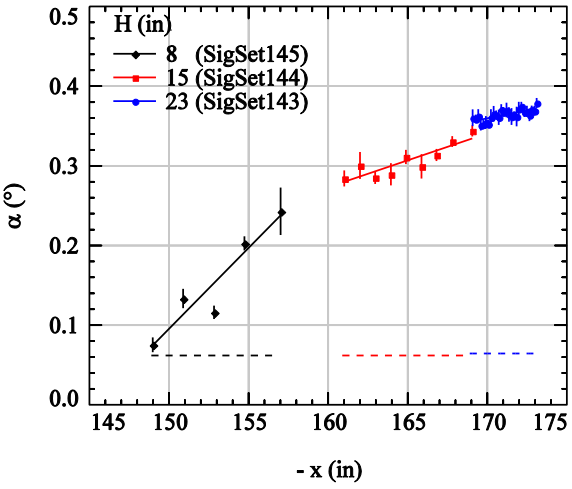

Figure 17. Effect of H_{nom} on α for double wedge.
M = 2.0; α_{nom} = 0°; NPR = 10.

increased α_{PG} and H_{PG} but had little effect on y_{PG} or the slopes $\Delta\alpha_{PG}/\Delta x$ and $\Delta H_{PG}/\Delta x$ (Fig. 11). Blowing had a smaller effect on α_{SDS}, H_{SDS}, and y_{SDS}.

How can we explain the increase in α_{PG} as the model moved upstream? Figure 10 (top) shows that this effect was not due to blowing. A lifting force on the model would create a pitching moment about the center of rotation that would cause both α and H to increase. However, a lifting force on a body of revolution at α = 0° was not expected. If lift was present and it remained constant as the x-ram was extended, both α and H would increase with increasing x because of the longer moment arm; however, if the model support is treated as a simple cantilever beam and the lift is treated as a concentrated load, the deflection would be a cubic function of x, not linear, and the angle at the free end would be a quadratic function of x.[19] Furthermore, the nonlinear behavior would be exacerbated if the lift increased as α increased.

The behavior of α_{PG} vs x could be due to a bias error in the photogrammetry measurements. A bias error could arise if the camera calibrations did not accurately represent the transformations from 3-D object space to the 2-D image plane of each camera (Eq. 1). One way to assess this error is to use photogrammetry to measure the space coordinates of targets whose space coordinates are known by other means, for example, the wall targets that were used to compute the pose of each camera (Fig. 8) and whose coordinates were measured by V-STARS. Table 1 shows the mean and rms differences between the photogrammetry and V-STARS coordinates of the 20 wall targets that were visible to both cameras. The errors are small, and the largest error is in the direction of the cameras (z), as expected. As another check on the photogrammetry, the space coordinates of two identifiable points on the outboard edge of the pressure rail near its upstream end were computed. Theoretically, the y and z coordinates of these points were the same; the difference between them as measured by photogrammetry was less than 0.01 in in both directions.

It is unlikely that there were systematic errors in locating the targets. A reprojection error was computed for each measurement of each target, and this error increased noticeably when a target was not properly located in the image from either camera. By monitoring the largest reprojection errors in each pair of images, we were able to insure that all targets were properly identified.

The uncertainty in each of the six degrees of freedom (model position and attitude) due to random errors in locating the targets in the images was estimated by:[20] (1) perturbing the image coordinates of each target in each image, one at a time, by the expected uncertainty; (2) summing the square of the changes in each of the six degrees of freedom produced by each perturbation; and (3) taking the square root of each sum. This procedure assumes that the image-plane uncertainties at all the targets are equal and independent of each other. A reasonable uncertainty in locating targets was 0.1 pixels. The corresponding random-error uncertainties for a typical case computed using all visible targets are shown in the second column of Table 1. Uncertainties were significantly larger (but still small) when model position and attitude were computed using only three targets (one near the nose and two near the nozzle). The relatively large uncertainty in roll occurred because all of the model targets were very close to the roll axis (x).

Table 1. Tabulated uncertainties.

	Calibration Error (pose images, in) 20 targets		Random Error (in) (Run 2161, 0.1 pixel uncertainty)	
	Mean	RMS	All targets (41)	3 targets
x (in)	0.002	0.047	0.0026	0.0069
y (in)	0.0005	0.023	0.0188	0.158
z (in)	0.012	0.110	0.0114	0.0279
α (°)	-	-	0.005	0.012
Yaw (°)	-	-	0.004	0.0063
Roll (°)	-	-	0.030	0.298

VII. Conclusion

The photogrammetry system performed as planned and provided model position and attitude measurements for 104 of 163 x-sweeps. Semi-automatic (human-assisted) data analysis was successfully accomplished in thousands of images. The analysis was seriously retarded, however, because the lighting and visibility of the targets was not optimal. Most notably, the bright RBOS background interfered with the target-finding algorithm resulting in many errors in locating targets that had to be corrected manually. The photogrammetry measurements showed unexpected changes in the position and attitude of the model as the model traversed upstream. If these trends are real, the photogrammetry data could make an important difference in how the pressure-rail data are interpreted.

Acknowledgments

The authors thank: Peter Coen, program manager of the Commercial Supersonics Technology (CST) Project, for supporting this work; Eduardo Solis of the Aeromechanics Office for measuring the space coordinates of the calibration targets with V-STARS; test director Steve Buchholz for accommodating our instrumentation and integrating our measurements into the test plan; and Tom Romer of the Wind Tunnel Systems Branch for discuaaing and coordinating SDS measurements of model position and attitude.

References

[1]Durston, D.A., et al., "Nozzle Plume/Shock Interaction Sonic Boom Test Results from the NASA Ames 9- by 7-Foot Supersonic Wind Tunnel," AIAA Paper presented at 43rd Aerospace Sciences Meeting and Exhibit, Grapevine, TX, Jan. 9–13, 2017.

[2]Brooks, J.D., and Beamish, J.K., "Measurements of Model Aeroelastic Deformations in the Wind Tunnel at Transonic Speeds Using Stereophotogrammetry," NASA TP 1010, July, 1977.

[3]Burner, A.W., Fleming, G.A., and Hoppe, J.C., "Comparison ofr Three Optical Methods for Measuring Model Deformation," AIAA Ppaper 2000-0835 presented at the 38th Aerospace Sciences Meeting and Exhibit, Reno, NV, Jan. 10–13, 2000.

[4]Quix, H., and Semmelmann, J., "Model Deformation Measurement Capabilities at ETW," AIAA Paper 2015–2562, presented at 31st AIAA Aerodynamic Measurement Technology and Ground Testing Conference, Dallas, TX, June 22-26, 2015.

[5]McDevitt, T.K., and Owen, F.K., "An Optical Angle of Attack Sensor," IEEE AES Magazine, Feb., 1990.

[6]Owen, F.K., McDevitt, T.K., Morgan, D.G., and Owen, A.K., "Wind Tunnel Model Angle of Attack Measurement using an Optical Model Attitude System," AIAA Paper 2000-16312 presented at 38th Aerospace Sciences Meeting and Exhibit, Reno, NV, Jan. 10–13, 2000.

[7]Lee. G., "Study of Optical Techniques for the Ames Unitary Wind Tunnels. Part 3. Angle of Attack Progress Report," NASA-CR-190541, June, 1992.

[8]Schairer, E.T., Kushner, L.K., Garbeff, T.J., and Heineck, J.T., "Model Deformation Measurements of Sonic Boom Models in the NASA Ames 9- by 7-Ft Supersonic Wind Tunnel", AIAA 2015-1913 presented at 53rd AIAA Aerospace Sciences Meeting, Kissimmee, FL, Jan 5–9, 2015.

[9]Drain, B.A., Schairer, E.T., Kushner, L.K., and Heineck, J.T., "Model Deformation Measurements of the Truss-Braced Wing Aircraft in the NASA Ames 11-By 11-Ft Transonic Wind Tunnel ," AIAA Paper presented at 43rd Aerospace Sciences Meeting and Exhibit, Grapevine, TX, Jan. 9–13, 2017.

[10]Raffel, M, "Background-oriented Schlieren Techniques," *Experiments in Fluids*, Vol. 56, No. 60, Mar. 2015.

[11]Anonymous, Standard Data System Wind Tunnel Data Reduction Equations High Speed Facilities, version 5, May 2000, Document Number A027-9891-XB3. The official version of this document is on the FO Web Server. (http://pubsgroup.arc.nasa.gov/FOPage/FOIBranchDocs.html).

[12]Schairer, E.T., Heineck, J.T., Walker, S.M., and Yaste, D. M., "Predicting Camera Views for Image-Based Measurements in Wind Tunnels," AIAA Paper 2005-1349, presented at 43rd Aerospace Sciences Meeting and Exhibit, Reno, NV, Jan. 10–13, 2005.

[13]Kushner, L.K. and Schairer, E.T., "Planning Image-Based Measurements in Wind Tunnels by Virtual Imaging," AIAA Paper 2011-0930, presented at 49th AIAA Aerospace Sciences Meeting and Exhibit, Orlando, FL, Jan., 2011.

[14]Mikhail, E.M., Bethel, J.S., and McGlone, J.C., *Introduction to Modern Photogrammetry*, Wiley and Sons, New York, 2001.

[15]Zhang, Z., "Flexible Camera Calibration by Viewing a Plane from Unknown Orientations," presented at International Conference on Computer Vision, Corfu, Greece, Sept. 1999, pp. 666–673.

[16]http://www.geodetic.com/products/systems/v-stars-s.aspx [cited 7 December 2016].

[17]Press, W.H. et al., *Numerical Recipes, The Art of Scientific Computing*, Cambridge University Press, Cambridge, 1986, pp. 523–528.

[18]Abdel-Aziz, Y.I., and Karara, H.M, "Direct Linear Transformation from Comparator Coordinates into Object-Space Coordinates," Proceedings of the Symposium on Close-Range Photogrammetry, Urbana, IL, January 1971.

[19]Timoshenko, S., and Young, D.H., *Elements of Strength of Materials*, Van Nostrand Reinhold Co., New York, 1968, p. 212.

[20]Holman, J.P., *Experimental Methods for Engineers*, McGraw-Hill Book Company, New York, 1966, pp. 37–38.